Asian Journal of Pharmaceutical Sciences 20 (2025) 101018

Available online at www.sciencedirect.com

ScienceDirect

journal homepage: www.elsevier.com/locate/AJPS

Research article

Tumor-specific liquid metal nitric oxide nanogenerator for enhanced breast cancer therapy

Chen Su[a,1], *Jianhan Lin*[b,1], *Cong Li*[f,1], *Xinyu Wang*[b], *Donghui Pan*[b], *Lizhen Wang*[b], *Yuping Xu*[b], *Chongyang Chen*[b], *Kangfan Ji*[c], *Jinqiang Wang*[c], *Daozhen Chen*[a,*], *Min Yang*[b], *Zhen Gu*[c,d,e,*], *Junjie Yan*[b,*]

[a] *Wuxi Maternal and Child Health Hospital, Wuxi School of Medicine, Jiangnan University, Wuxi 214002, China*
[b] *NHC Key Laboratory of Nuclear Medicine, Jiangsu Key Laboratory of Molecular Nuclear Medicine, Jiangsu Institute of Nuclear Medicine, Wuxi 214063, China*
[c] *Key Laboratory of Advanced Drug Delivery Systems of Zhejiang Province, College of Pharmaceutical Sciences, Zhejiang University, Hangzhou 310058, China*
[d] *Department of General Surgery, Sir Run Run Shaw Hospital, School of Medicine, Zhejiang University, Hangzhou 310016, China*
[e] *MOE Key Laboratory of Macromolecular Synthesis and Functionalization, Department of Polymer Science and Engineering, Zhejiang University, Hangzhou 310027, China*
[f] *The affiliated Wuxi People's Hospital of Nanjing Medical University, Wuxi Medical Center, Nanjing Medical University, Wuxi People's Hospital, Wuxi 214023, China*

ARTICLE INFO

Article history:
Received 2 July 2024
Revised 2 December 2024
Accepted 9 December 2024
Available online 10 January 2025

Keywords:
Liquid metal
Nitric oxide
Gas therapy
Cancer treatment
Nanomedicine

ABSTRACT

Nitric oxide (NO) modulates several cancer-related physiological processes and has advanced the development of green methods for cancer treatment and integrated platforms for combination or synergistic therapies. Although a nanoengineering strategy has been proposed to overcome deficiencies of NO gas or small NO donor molecules, such as short half-life, lipophilicity, non-selectivity, and poor stability, it remains challenging to prepare NO nanomedicines with simple composition, multiple functions and enhanced therapeutic efficacy. Herein, we build a liquid metal nanodroplet (LMND)-based NO nanogenerator (LMND@HSG) that is stabilized by a bioreducible guanylated hyperbranched poly(amido amine) (HSG) ligand. Mechanically, the tumor microenvironment specifically triggers a cascade process of glutathione elimination, reactive oxygen species (ROS) generation, and NO release. According to actual demand, the ROS and NO concentrations could be readily controlled by tuning the LMND and HSG feed amounts. Along with the intrinsic anticancer property of LMND (ROS-mediated apoptosis and anti-angiogenesis), LMND@HSG administration could further enhance tumor growth suppression compared with LMND and

* Corresponding authors.
E-mail addresses: 9862022077@jiangnan.edu.cn (D. Chen), guzhen@zju.edu.cn (Z. Gu), yanjunjie@jsinm.org (J. Yan).
[1] These authors contribute equally.
Peer review under responsibility of Shenyang Pharmaceutical University.

https://doi.org/10.1016/j.ajps.2025.101018

HSG alone. From this study, leveraging LMND for NO gas therapy provides more possibilities for the prospect of LMND-based anticancer nanomedicines.

1. Introduction

Nitric oxide (NO) gas therapy has arisen as a prospective cancer treatment approach owing to its advantages of mitigated toxicity, short treatment duration, viable to drug resistance, multiple mechanistic pathways (e.g., nitrite stress, mitochondrial/DNA damage, apoptosis, et al.) [1–6], and synergism with other therapeutic modalities including chemotherapy, radiotherapy, photodynamic therapy, immunotherapy, etc. [7–11]. However, direct utilization of NO gas or small NO donor molecules is hampered by its lipophilicity, purposeless diffusion, instability, short half-life (2-5 s), and vulnerability to bioactive substances as reactive oxygen species (ROS), glutathione (GSH), and hemoglobin [9,12]. In this context, the strategy of nanoengineering NO-delivering systems, such as encapsulating, surface engineering and self-assembling of NO-donors on or into nanomaterials [3,13–15], has been developed to accomplish controllable NO loading, delivery/release and therapy, simultaneously facilitating the introduction of other anticancer agents for combination or synergistic therapy.

Generally, the ideal nanomaterials for integrating NO donors involve the following physicochemical characteristics. First, the composition of the nanomaterials should be simple and biocompatible. To provide NO delivery nanosystems with multiple performances, either various cargoes or complex nanostructures are usually demanded, which will pose challenges for the synthesis, *in vivo* stability of nanomaterials, and evaluation of combined or synergistic effects between components. Second, stimuli-responsiveness is often necessary to obtain spatiotemporally selective NO release/therapy with minimal invasiveness. Although the tumor microenvironment (TME) could supply endogenous stimuli, including hydrogen peroxide (H_2O_2), GSH, pH, glucose, etc. [16,17], the low availability of H_2O_2 (< 100 μM) and high levels of intracellular GSH (1–10 mM) in the TME would fail to provide sufficient ROS to activate NO generation. On the other hand, exogenous stimuli basically rely on the employment of external energy input, such as heat, light, X-ray, and ultrasound [18,19], and such use scenarios would limit further clinical translation [4]. Besides, flexible regulation of ROS in nanomaterials is very important. Although fertile ROS aids in NO activation for gas therapy [7,20–22], the inflammation risk cannot be ignored.

Gallium (Ga)-based liquid metal nanodroplets (LMNDs) have been widely studied as an emerging class of metal-based nanomaterials because of their good biocompatibility and low cytotoxicity [23–25]. LMND could release ROS upon degrading into Ga^{3+} ions in living objects [26–29], continuously producing abundant ROS and participating in various physiological processes. The sonochemical energy during the sonosynthesis can also be stored for additional ROS generation by surface engineering [30]. More importantly, we recently found that the abundant ROS in LMNDs could potentiate cancer therapy through dual mechanisms of apoptosis and anti-angiogenesis [31], and Kalantar-Zadeh's group reported that gallium nanodroplet could escape from inflammation by disturbing the synthesis of NO synthase in macrophages [32]. Therefore, LMNDs modified with appropriate ligands could regulate the ROS status in the TME and potentially enroll NO gas therapy with sensitization [33–34]. Despite these priorities, LMND-based gas therapy has not been studied yet.

Herein, we employed bioreducible guanylated hyperbranched poly(amido amine) (HSG) as a stable ligand for LNMD through multivalent amine-gallium binding interactions, in which the disulfide bonds and guanidino groups in HSG deplete excessive GSH in the TME and act as NO donors, respectively. Notably, the constructed LMND NO nanogenerator presented the cascade self-supply systems of ROS and NO. ROS was generated by LMNDs and maximumly retained via the GSH depletion strategy by disulfide bonds, which subsequently triggered NO release from the guanidino groups (Fig. 1). The LMND@HSG nanomedicine exhibited significantly enhanced therapeutic efficacy compared to ROS and NO therapy alone. This is the first LMND-based nanogenerator for NO gas therapy, and the intrinsic anticancer and anti-inflammation activities of LMND provide a platform for combination/synergistic therapy and advance the understanding of mechanisms.

2. Materials and methods

2.1. Materials

Gallium Indium eutectic (EGaIn, Alfa Aesar, 99.99%), cystamine dihydrochloride (Sigma-aldrich, 98%), acryloyl chloride (TCI, 97%), *N*-aminoethylpiperazine (AEPZ, TCI, ≥98%), *N,N'*-methylenebisacrylamide (MBA, Alfa, >99%), 1H-pyrazole-1-carboxamidine hydrochloride (TCI, 98%), *N,N*-diisopropylethylamine (DIPEA, Alfa, 99%). Unless otherwise stated, all test kits were provided by Beyotime Biotechnology (Shanghai, China). 4T1 cells were derived from the Cell Bank of the Chinese Academy of Sciences. All animal experiments were approved by the Animal Ethics Committee of Jiangsu Institute of Nuclear Medicine (No. JSINM-2023-032) and followed corresponding guidelines.

2.2. Characterizations

Nuclear magnetic resonance (NMR) was characterized using a Bruker Avance II 400 spectrometer. The average molecular

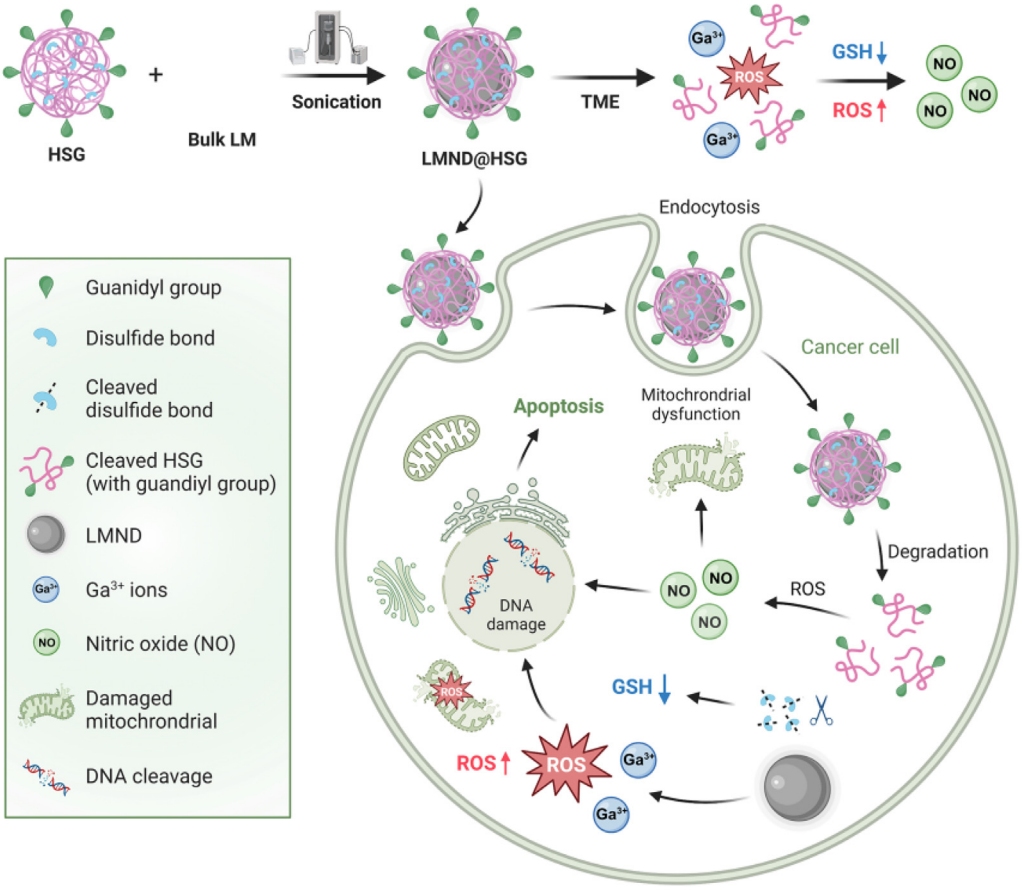

Fig. 1 – Schematic illustration of cancer therapy mechanism of LMND@HSG nanomedicine. LMND@HSG could generate ROS in the TME and deplete endogenous GSH to promote ROS retention. Enhanced ROS accessibility in the TME would facilitate NO release for combined cancer therapy, causing simultaneous DNA double-strand breaks and mitochondrial dysfunction, ultimately leading to the apoptosis of tumor cells.

weights of the polymers were carried out on a Breeze2 gel permeation chromatography (GPC) system (Waters). Dimethylformamide (DMF) was utilized as an eluent at a flow rate of 1 ml/min, temperature: 35 °C. Polystyrene was utilized as calibration. The hydrodynamic sizes of nanomaterials and surface potentials were tested on a Zetasizer Nano ZS90 particle size analyzer (Marlvern). X-ray diffraction (XRD) measurement was determined on a Bruker D8 Advance XRD diffractometer. X-ray photoelectron spectrometer (XPS) analysis was performed on a Thermo ESCALAB 250XI XPS Microprobe. The morphology of LMND@HSG nanodroplets was tested on a Tecnai G2 20 transmission electron microscopy (TEM). Fluorescent probe experiments were measured on a HORIBA FluoroMax Plus spectrofluorometer. Cell fluorescence experiments were carried out on a TH4-200 inverted fluorescence microscope (OLYMPUS).

2.3. *Synthesis of N,N'-bis(acryloyl)cystamine (CBA)*

CBA was synthesized in the following procedure (Fig. S1). Briefly, cystamine dihydrochloride (6.80 g, 30.0 mmol) and NaOH (5.20 g, 130.0 mmol) were added into 150 ml deionized water, and acryloyl chloride (6.40 g, 70.0 mmol, dissolved in 6 ml chloroform) was added dropwise. Then, the mixture was vigorously stirred in an ice bath for 6 h. The raw product was filtrated and rinsed thrice with deionized water. Then, the mixed solution was extracted with dichloromethane thrice (3 × 100 ml). After that, the organic phase solution was dried with anhydrous Na_2SO_4, and vacuum extracted at room temperature. CBA was finally purified by recrystallization in ethyl acetate at a yield of 67.4%.

2.4. *Synthesis of hyperbranched poly(amido amine) (HPAA) and bioreducible HPAA (HPAP)*

HPAA and HPAP (with disulfide groups) were prepared using the Michael addition reaction (Fig. S1). (i) For HPAA, AEPZ (258.3 mg, 2.00 mmol) and MBA (616.9 mg, 4.00 mmol) (molar ratio: AEPZ/MBA = 1:2), (ii) for HPAP condition, AEPZ (258.4 mg, 2.00 mmol), MBA (462.7 mg, 3.00 mmol) and CBA (260.4 mg, 1.00 mmol) (molar ratio: AEPZ to MBA to CBA = 2:3:1) were dissolved in mixed solvents of methanol/water (8.0 ml, v/v = 7/3). The reaction mixture was placed at 50-55 °C for 120 h. Afterwards, AEPZ (361.7 mg, 2.80 mmol) was used to terminate the acrylamide groups of HPAA and HPAP at 37 °C for 8 h. The raw products were purified by precipitating in cold acetone, followed by vacuum drying for 2 h at room temperature.

2.5. Guanylation of hyperbranched poly(amido amine)

HPAA and HPAP (1.0 g) were dissolved in 15 ml methanol, respectively. Then 1H-pyrazole-1-carboxamidine hydrochloride (410.4 mg, 2.80 mmol) and DIPEA (361.9 mg, 2.80 mmol) were added dropwise. The mixture was reacted at room temperature for 48 h, followed with 72 h dialysis against cold deionized water, and collected by freeze-drying finally.

2.6. Preparation of LMND@HSG

EGaIn (80 μl) and HSG solution (5 mg, 12 ml) were added into a centrifuge tube, and the reaction mixture was sonicated in an ice bath for 12 min. After that, large nanodroplets were thrown away by centrifugating for 5 min (1,200 rpm). After the reaction, the concentration of LMND@HSG was set up using a lyophilization approach. The quantification of Ga in LMND@HSG was determined by ICP-MS (Agilent 7700X).

2.7. ROS Detection in vitro

In deionized H_2O: DCFH-DA probe (10 μM) was mixed with LMND@HSG at different concentrations of H_2O_2 (0.1, 5 and 10 mM) for 40 min in the dark at 37 °C. After centrifugation (6,000 rpm, 5 min), the obtained supernatant was tested on a spectrofluorometer at the excitation/emission wavelengths of 488 nm (E_x488) and 525 nm (E_m525), respectively.

In cells: 4T1 cells were cultured in a 24-well plate (2×10^4 cells per well). Subsequently, the cells were cultured with respective 10 μg/ml HSG, 40 μg/ml LMND, and 40 μg/ml LMND@HSG. After an additional 4 h incubation, the resultant cells were gently washed thrice with PBS and then reacted with DCFH-DA (10 μM) for 40 min. Finally, excess DCFH-DA was removed and the cell nuclei were stained with Hoechst 33342. Finally, the cellular fluorescence was recorded on a fluorescence microscope.

2.8. NO Detection in vitro

In deionized H_2O: HSG (0.5 mg/ml) and LMND@HSG (2 mg/ml) with or without 10 mM H_2O_2 were reacted with a DAF FM-DA probe (5 μM) for 24 h at 37 °C, respectively. After the probe was co-incubated with LMND@HSG, the nanodroplets were discarded by centrifugation, and the supernatant solution was utilized for the fluorescence test. When the concentration of LMND@HSG exceeded 2 mg/ml, the transmittance of the supernatant was too poor to qualify the data validity. Therefore, the concentration of LMND@HSG was set at 2 mg/ml. Based on the composition of LMND@HSG, the concentration of HSG should be theoretically set at 0.02 mg/ml. However, to exclude the NO contribution from HSG in the absence of LMND, we applied an excess amount of HSG and set its concentration at 0.5 mg/ml. The collected supernatant was measured at E_x495 and E_m515 on a spectrofluorometer.

In cells: 4T1 cells were cultured in a 24-well plate (2×10^4 per well). Then, 10 μg/ml HSG, 40 μg/ml LMND, and 40 μg/ml LMND@HSG were fed into cells, respectively. After incubation for 4 h, the resultant cells were gently washed with PBS and reacted with 5 μM DAF-FM DA for 24 h. Finally, excess free DAF-FM DA were removed by PBS washing thrice and the cells were additionally stained with Hoechst 33342. Finally, the cellular fluorescence was recorded on a fluorescence microscope.

2.9. In vitro reaction between HSG and GSH

The consumption of GSH was analyzed by 5,5′-dithiobis-(2-nitrobenzoic acid) (DTNB) to quantitate thiols in target molecules. Briefly, GSH (2 mM) was mixed with an equal solution of samples for 12 h at room temperature (HSG: 2 mg/ml). An aliquot of 6.6 μl aqueous DTNB solution was diluted with 150 μl Tris-HCl and mixed with the above reaction mixtures for 15 min. Finally, the reaction components were identified utilizing high performance liquid chromatography (HPLC).

2.10. Immunofluorescence

The DNA double-strand breaks were investigated using immunofluorescence staining of γ-H2AX. 4T1 cells were cultured at a density of 2×10^4 cells per well in a 24-well plate, then 10 μg/ml HSG, 40 μg/ml LMND and 40 μg/ml LMND@HSG were added, respectively. After the incubation for 24 h, the treated cells were rinsed with PBS and incubated with 4% paraformaldehyde. Subsequently, fixed cells were treated with 0.25% Triton X-100 and immunofluorescence blocking buffer solution for 20 min. γ-H2AX rabbit monoclonal antibody (C2036S, Beyotime Biotechnology) was incubated with cells at 4 °C overnight. After that, the secondary antibody was further incubated with cells for additional 1 h, and the cell nucleus was stained with Hoechst 33342. Finally, the fluorescent images of cells were captured on a fluorescence microscope.

2.11. Intracellular mitochondrial damage detection in 4T1 cells

4T1 cells were plated into a 24-well plate (2×10^4 cells per well). Then, 10 μg/ml HSG, 40 μg/ml LMND, and 40 μg/ml LMND@HSG were cultured with cells, respectively. After the incubation for 24 h, the resultant cells were rinsed with PBS thrice and later cultured with Mito-Tracker probe (Beyotime Biotechnology) for 30 min. The mitochondrial damage of cells was characterized on a flow cytometer and a fluorescence microscope.

2.12. Cytotoxicity of LMND@HSG against 4T1 cells

4T1 cells were plated into a 96-well plate (6×10^3 per well). Subsequently, the cells were fed with varying concentrations (0, 2, 5, 10, 20, 40, 80, 160 and 320 μg/ml) of LMND@HSG for 24 h. After that, 10 μl MTT solutions were further added and cultured for an additional 2 h. Finally, the characteristic absorbance at 490 nm was measured on a microplate reader.

2.13. Cell apoptosis of LMND@HSG against 4T1 cells

Live/dead cell viability assay: 4T1 cells were cultured in a 24-well plate (2×10^4 per well). Subsequently, 10 μg/ml HSG, 40 μg/ml LMND, and 40 μg/ml LMND@HSG were separately

incubated with 4T1 cells for 24 h. Afterward, the treated cells were incubated with calcein acetoxymethyl ester (Calcein-AM) and propidium iodide (PI). After 30 min, the cells were investigated using a fluorescence microscope.

Annexin V-FITC/PI assay: 4T1 cells were cultured at a density of 1×10^5 cells per well into a 6-well plate. After 24 h, 10 μg/ml HSG, 40 μg/ml LMND and 40 μg/ml LMND@HSG were respectively added to incubate with the cells. Another 24 h later, the cells were collected by trypsin. Finally, the collected cells were incubated with Annexin V-FITC/PI assay in a centrifuge tube for 0.5 h and subjected to flow cytometry measurement. The data were processed via FlowJo V10 software.

2.14. *Animal models*

All animal experiment protocols used in this study were authorized with permission from the Animal Care and Ethics Committee of Jiangsu Institute of Nuclear Medicine. The female BALB/c mice (5–6 wk, weighed 18-22 g) were obtained from Cavens Laboratory Animal Co. (Changzhou, China). The 4T1 mice model was established by subcutaneous injection of luciferase-tagged 4T1 (4T1-luc) cells (1×10^6) into the flank of BALB/c mice. The formula for calculating tumor volume (mm^3) in mice is 0.5 × length × width [2]. When tumor volumes approached a predetermined number, the mice were randomly assigned to predetermined groups for further experiments.

2.15. *In vivo treatment efficacy*

For the evaluation of the *in vivo* treatment efficacy of various formulations, 2 mg/kg HSG, 2 mg/kg LMND, 2 mg/kg LMND@HPAA and 2 mg/kg LMND@HSG and saline were intratumorally injected into 4T1 tumor-bearing mice every other day. After 14-d treatment, or the tumor volume reached nearly 1,000 mm^3, mice were executed. The tumor and main organs (heart, liver, spleen, lung, and kidneys) were separated for further analysis and characterizations.

2.16. *Statistical analysis*

The statistics were processed by SPSS 24.0 software. All the results were represented to be mean ± standard deviation (SD) ($n \geq 3$). For two-group and multiple comparisons, a two-tailed Student's t-test and one-way analysis of variance (ANOVA) were used, respectively. $P < 0.05$ indicates a significant difference, and ns shows no significance.

3. Results and Discussion

3.1. *Synthesis of NO donor ligand HSG*

HPAA was synthesized based on previous literature [35,36]. As revealed in Fig. 2A, different molar ratios of bisacrylamide (MBA and CBA, n/n: 1/0, 5/1, 4/1, 3/1) with AEPZ (half the molar amount of bisacrylamide) were applied to occur Michael addition reaction in solvents of water and methanol (7/3, v/v). Different radios of CBA and MBA regulate the content of disulfide bonds, which could alter the hydrophilicity, bioreducibility, and solubility of resultant polymers. Additional AEPZ was used to terminate the acrylamide end groups, affording HPAA and HPAP. As the topological architectures of PAA could be readily modulated by varying the polymerization parameters including molar feed ratio, solvent, temperature, etc. [37], the polymerization conditions were strictly controlled. The chemical structures of HPAA and HPAP were verified by ^{1}H NMR spectra (Fig. S2). The typical protons of the double bonds of acrylamides vanished, indicating the complete AEPZ termination. With increasing CBA feed ratio (HPAP31>HPAP41>HPAP51>HPAA10), corresponding HPAP had increased signals of methylene protons at 2.78 ppm (marked with blue stripe) in the ^{1}H NMR spectra, and MBA methylene protons at 4.35 ppm (marked with red stripe) were set as the reference. To further attach the guanidino group at the terminal of HPAA/HPAP, 1H-pyrazole-1-carboxamidine monohydrochloride was used to guanylate HPAA/HPAP and the resultant products HSG had typical signals of guanidine protons at 7.83-8.35 ppm (marked with cyan stripe) in the ^{1}H NMR spectra (Fig. 2B). The GPC curves indicated that HSG had increased molecular weights compared to HPAP after the guanylation (Fig. 2C). Moreover, FTIR spectra showed that the respective C-O stretch and C=O vibration bands at 1218 and 1708 cm^{-1} weakened after the guanylation [38], and the blue-shift of 1530 to 1522 cm^{-1} indicated the formation of -NH_2^+ bending (Fig. 2D) [39].

3.2. *Synthesis and characterizations of LMND@HSG*

The ligands are of great importance in stabilizing aqueous LMNDs. According to our previous study, HPAA could steady LMNDs through the surface absorption of tertiary amines [35]. Based on this, here we introduced disulfide bonds and guanidino groups within the structure of HPAA, namely HSG. HSG ligand could stabilize LMND and release NO from guanidino groups under ROS stimulation. Meanwhile, the presence of disulfide bonds could consume GSH and thus increase the retention of ROS. LMND@HSG was prepared from a sonosynthesis approach as shown in Fig. 3A. TEM images reveal that LMND@HSG has a spherical morphology with a polymeric layer coating (Fig. 3B&3C), and the overall size is 186.0 ± 16.4 nm. The DLS measurement shows that LMND@HSG has a hydrodynamic size of 212.7 ± 2.6 nm, surface zeta potential of +34.20 mV, and a narrow polydispersity index (PDI) of 0.11 (Fig. 3D). During 7-d monitoring, the hydrodynamic size and zeta potential did not occur significant changes, indicating good stability of LMND@HSG (Fig. 3E).

To verify the compositions of LMND@HSG, measurements of FTIR and XRD were performed. In the FTIR analysis (Fig. 3F), the similar spectra of HSG and LMND@HSG indicated the presence of HSG in the nanocomposites. XRD spectrum of LMND@HSG consists of individual pair distribution function analysis (PDF) cards of gallium oxide monohydroxide (GaO(OH)) and indium (In), confirming the compositions of LMND@HSG in agreement with previous studies (Fig. 3G). The XPS analysis was further utilized to investigate the interaction between LMND and HSG. Aside from primary elements of Ga, In, carbon, oxygen, and

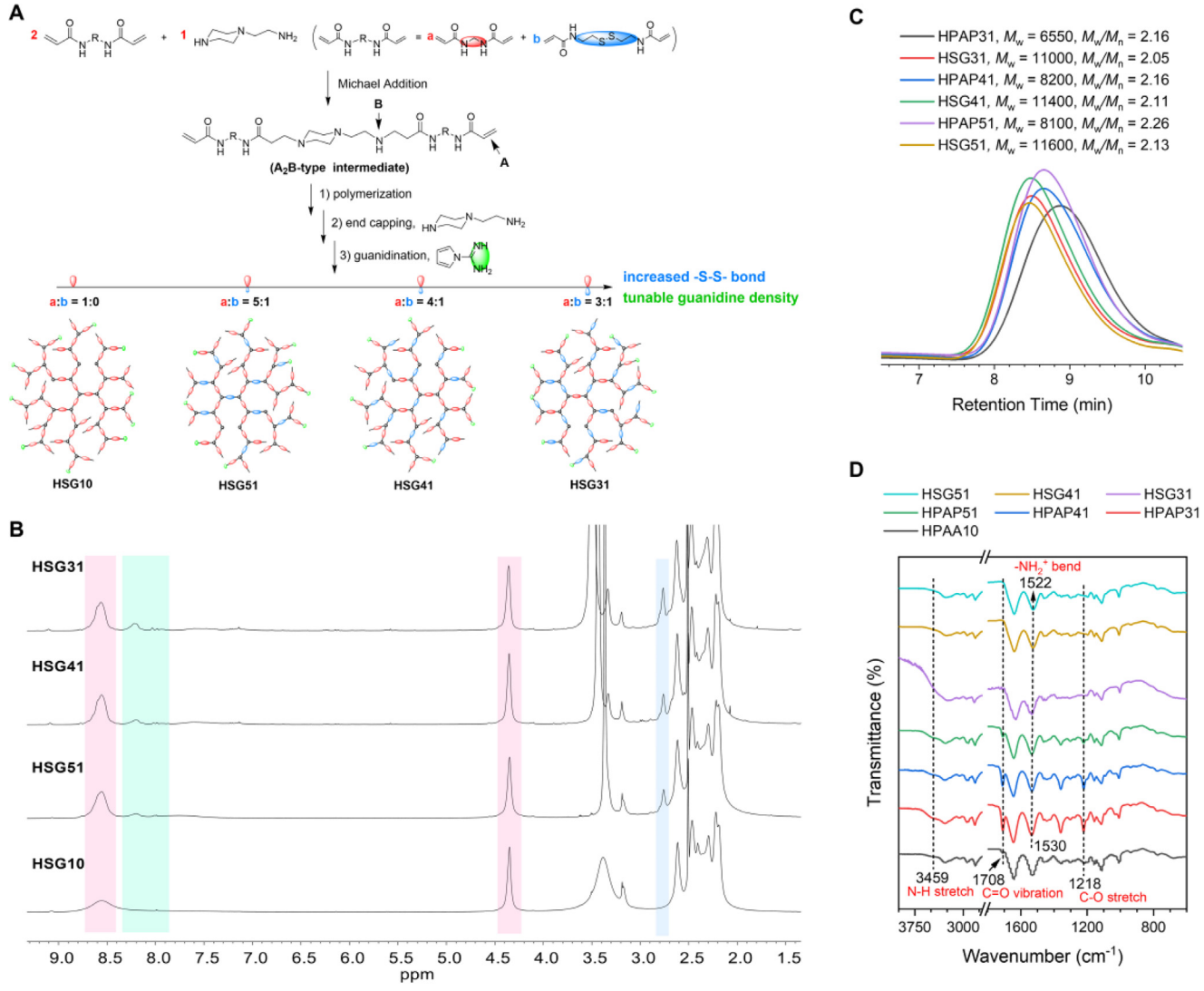

Fig. 2 – The synthetic route and characterizations of HSG ligands. (A) Structures of HSG with different content of disulfide bonds. (B) ^{1}H NMR spectra of HSG with different content of disulfide bonds. (C) GPC curves of HPAP and HSG with different content of disulfide bonds. (D) FTIR spectra of HPAP and HSG with different content of disulfide bonds.

nitrogen (Fig. S3A), in the Ga 3d high-resolution XPS spectrum, two signals at binding energies (BEs) of 17.3 and 19.5 eV were attributed to elemental Ga^0 and Ga (III), respectively, indicating the generation of a Ga oxide layer on surface of LMNDs (Fig. 3H). In the N 1s spectrum, three differentiating BEs at 399.1, 396.7, and 393.6 eV belonged to characteristic peaks of N-H, N-Ga (III), and Ga LMM, separately (Fig. 3I). For the C 1s condition, three deconvoluted peaks at BEs of 284.6 (C-C), 285.6 (C-N), and 287.4 eV (C=O) soundly match the types of carbon bonds in HSG (Fig. S3B). Collectively, these results verify that HSG was attached to the surface of LMNDs *via* the N-Ga binding, and thus, LMND@HSG nanocomposite was synthesized with a well-defined structure.

3.3. *In vitro ROS and NO release of LMND@HSG*

As illustrated in Fig. 4A, guanidino group-containing LMND@HSG could trigger ROS generation in acidic conditions, and disulfide bonds within the HSG skeleton could meanwhile deplete GSH in the TME to reduce ROS consumption. Consequently, such a cascade system could facilitate ROS supply and NO production, providing conditions for combined ROS-related chemotherapy and gas therapy. We used DCFH-DA and DAF-MF DA probes to examine the capabilities of LMND@HSG to produce ROS and NO, respectively. In the ROS test, H_2O_2 incubation alone (0.1, 5 and 10 mM) did not produce fluorescence, but the co-incubation with LMND@HSG generated fluorescence, indicating ROS generation (Fig. 4B). The higher concentration of H_2O_2, the stronger fluorescence intensity (FI) was. By contrast, the absence of H_2O_2 could only produce weak fluorescence upon LMND@HSG incubation alone. The results also revealed that the LMND had a weaker ability to generate ROS than the LMND@HSG group. At the same H_2O_2 concentration (10 mM), the amount of ROS generated by LMND is 17.7% of the LMND@HSG group. These results showed that ROS was mainly derived from LMND,

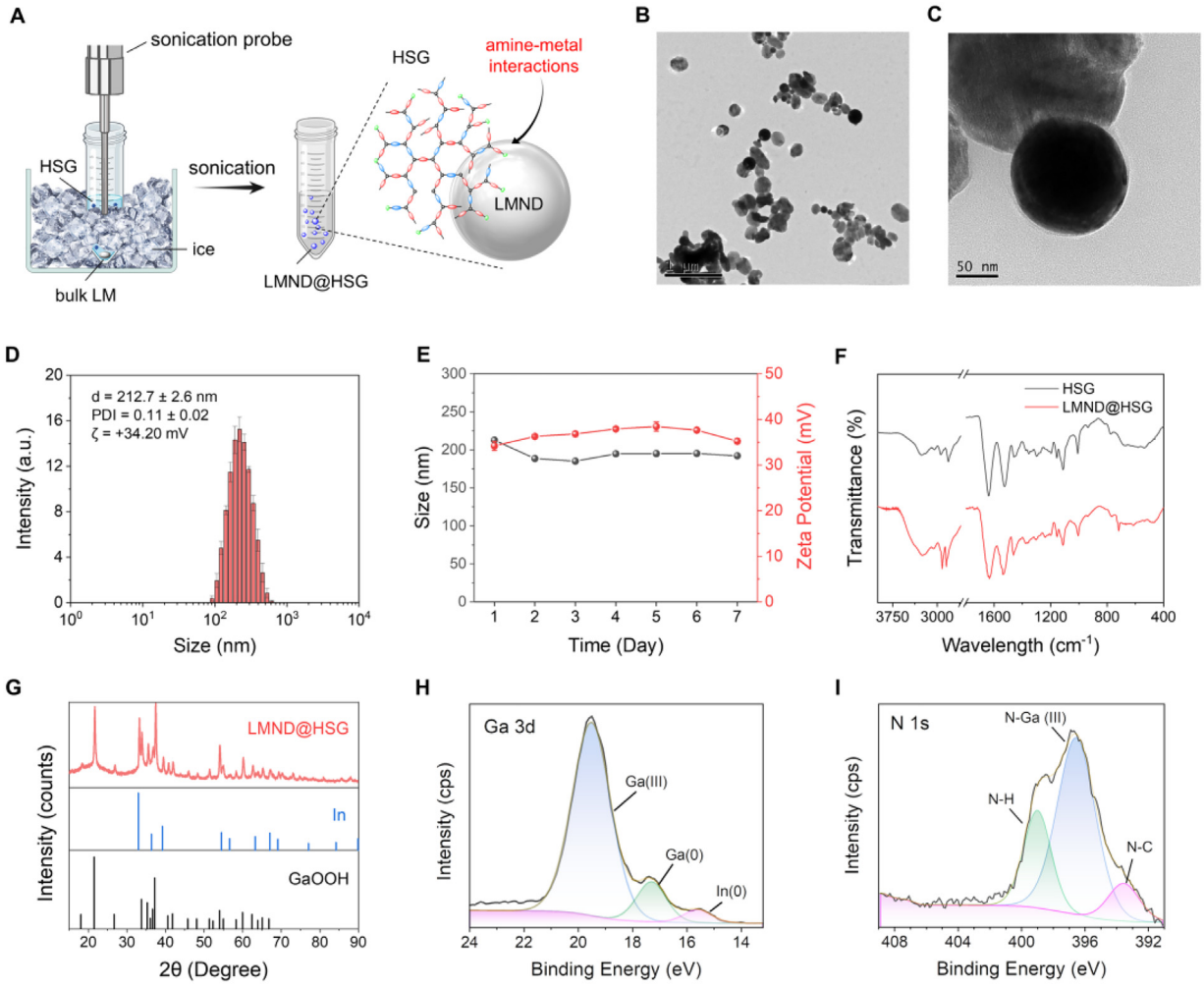

Fig. 3 – Synthesis and characterizations of LMND@HSG. (A) Schematic diagram of the synthesis of LMND@HSG. (B,C) TEM images of LMND@HSG. Scale bar: (B)1 μm and (C) 50 nm. (D) Size, PDI and ζ of LMND@HSG (40 μg/ml in water) measured by DLS. All data are expressed as mean ± SD ($n = 4$). (E) Size and ζ stability of LMND@HSG for 7 d in water. All data are expressed as mean ± SD ($n = 4$). (F) FTIR spectra of LMND@HSG and HSG. (G) XRD spectra of LMND@HSG, In and GaOOH. (H, I) High resolution Ga 3d and N 1s XPS spectra of LMND@HSG.

and H_2O_2 accelerated ROS generation due to the pH-induced degradation of LMND.

GSH is an important factor in regulating redox balance and could consume ROS, so disulfide bonds were introduced in the structure of HSG to deplete endogenous GSH in the TME. GSH and glutathione disulfide (GSSG) assay kit was applied to determine the GSH consumption capability of HSG. GSH can react with chromogenic substrate DTNB to yield yellow 2-nitro-5-thiobenzoic acid (TNB) and GSSG, and HPLC was used to monitor the composition of the reaction mixture. As shown in Fig. 4C and D, HSG10 could hardly consume GSH (0.2%). Upon increasing the content of disulfide bonds, the GSH consumption was raised and HSG31 consumed the highest level at 11.5%. Therefore, HSG31 was chosen as the optimal ligand, abbreviated as LMND@HSG in the following experiments and discussions. When 1 mM GSH was added, the ROS content reduced to 29.6% and 34.0% in LMND@HSG and LMND@HSG10 groups, respectively (Fig. 4E). LMND@HSG group retained more ROS compared with the LMND@HSG10 group because of the existence of disulfide bonds. To prove if retaining ROS could trigger NO generation in LMND@HSG, 5 μM DAF-MF DA was further reacted with aqueous solutions of HSG, HSG+10 mM H_2O_2, LMND@HSG, and LMND@HSG+10 mM H_2O_2, respectively. As depicted in Fig. 4F, LMND@HSG+10 mM H_2O_2 group showed the highest FI at E_m515, which indicated that HSG could yield NO more efficiently with the stimulations of LMND and H_2O_2.

Next, the production of ROS and NO at the cellular level was also investigated by confocal laser scanning microscopy (CLSM). Fig. 4G showed that the LMND@HSG-cultured group had the strongest cellular fluorescence in the DCFH-DA channel, and anticipated fluorescence was observed in the LMND-cultured group due to its energy storage performance [30]. By contrast, no apparent green fluorescence was detected in the HSG-cultured or control groups. Similarly, the NO cellular fluorescence study showed that only the LMND@HSG-

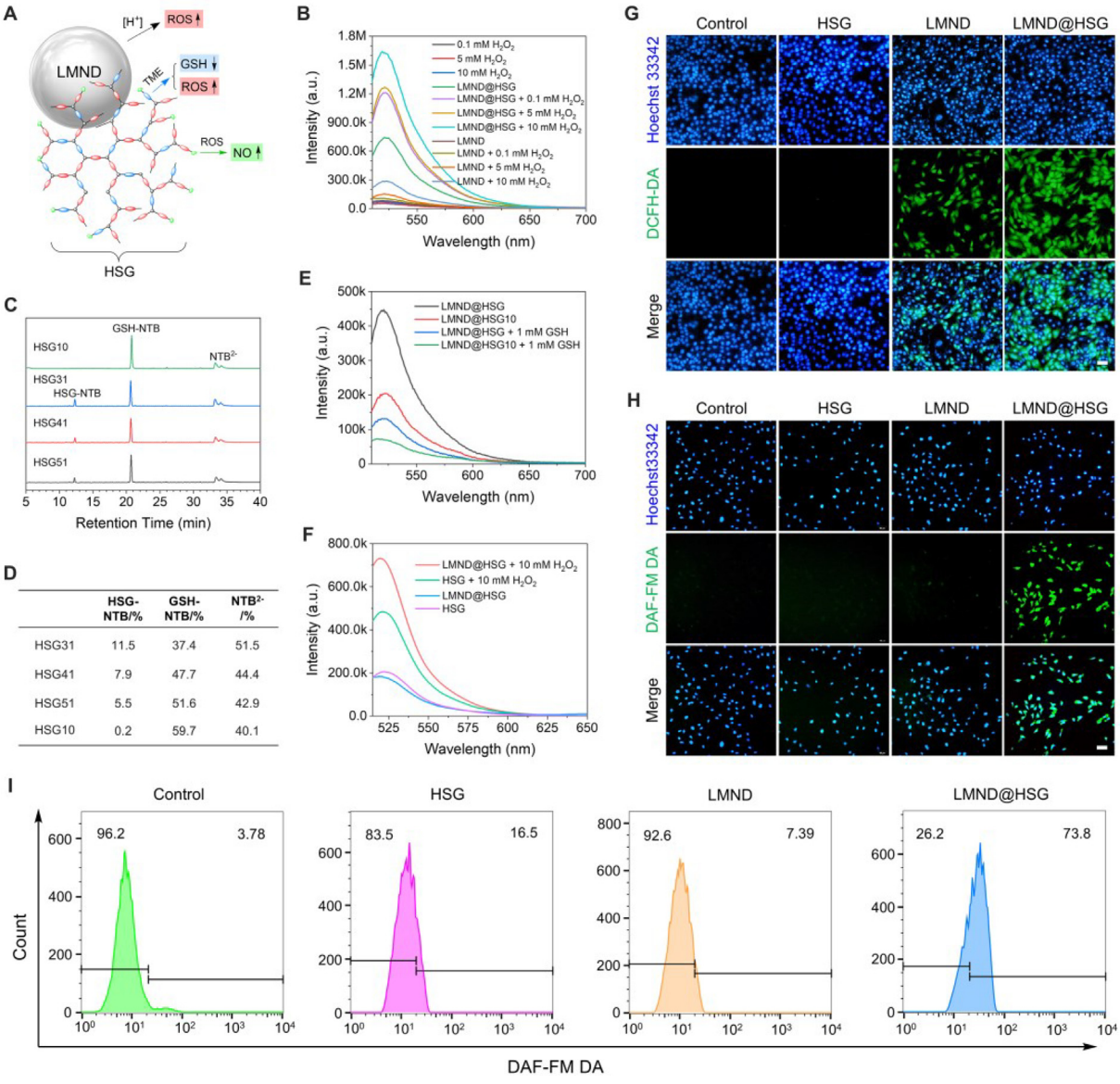

Fig. 4 – *In vitro* performance of LMND@HSG. (A) Schematic diagram of LMND@HSG in activating ROS and NO generation. (B) ROS generation of LMND@HSG with or without H_2O_2 stimulation. (C, D) Quantitative analysis of GSH consumption capacity of HSG by HPLC, and DTNB was used as the substrate. (E) ROS generation/retention of LMND@HSG in the presence of 1 mM GSH. (F) The influence of LMND and H_2O_2 on the NO generation/retention capability of HSG ligands. (G) DCFH-DA probe-mediated ROS generation test and (H) DAF-MF DA probe-mediated NO generation test of HSG, LMND and LMND@HSG in 4T1 cells. Scale bar: 50 μm. (I) DAF-MF DA probe-mediated NO generation test of HSG, LMND and LMND@HSG by flow cytometry.

cultured group could generate NO by the green fluorescence in the DAF-MF DA channel, revealing that LMND could be supplemented to increase the insufficient ROS level in the TME and thus trigger NO generation (Fig. 4H). The flow cytometry experiment also confirmed this trend, achieving the highest percentage of positive cells (DAF-MF DA staining) in the LMND@HSG group (Fig. 4I). Taken together, ROS was mainly generated by the acidic degradation of LMNDs in the TME and maximumly retained *via* the GSH depletion strategy by disulfide bond units, which subsequently triggered NO release from the guanidino groups.

3.4. *In vitro cytotoxicity of LMND@HSG*

To evaluate the cytotoxicity of LMNG@HSG, the methyl tetrazolium (MTT) assay was tested. LMND and HSG alone presented weak cytotoxicity (cell viability >73%) towards 4T1 at a concentration high up to 160 μg/ml (Fig. 5A), indicating their good compatibility. By contrast, LMND@HSG showed significant cytotoxicity, possessing a half-maximal inhibitory concentration (IC50) value of 29.76 μg/ml toward 4T1 cells, which was comparable to that of small-sized (<30 nm) LMND [31]. The combination index (CI) values shown

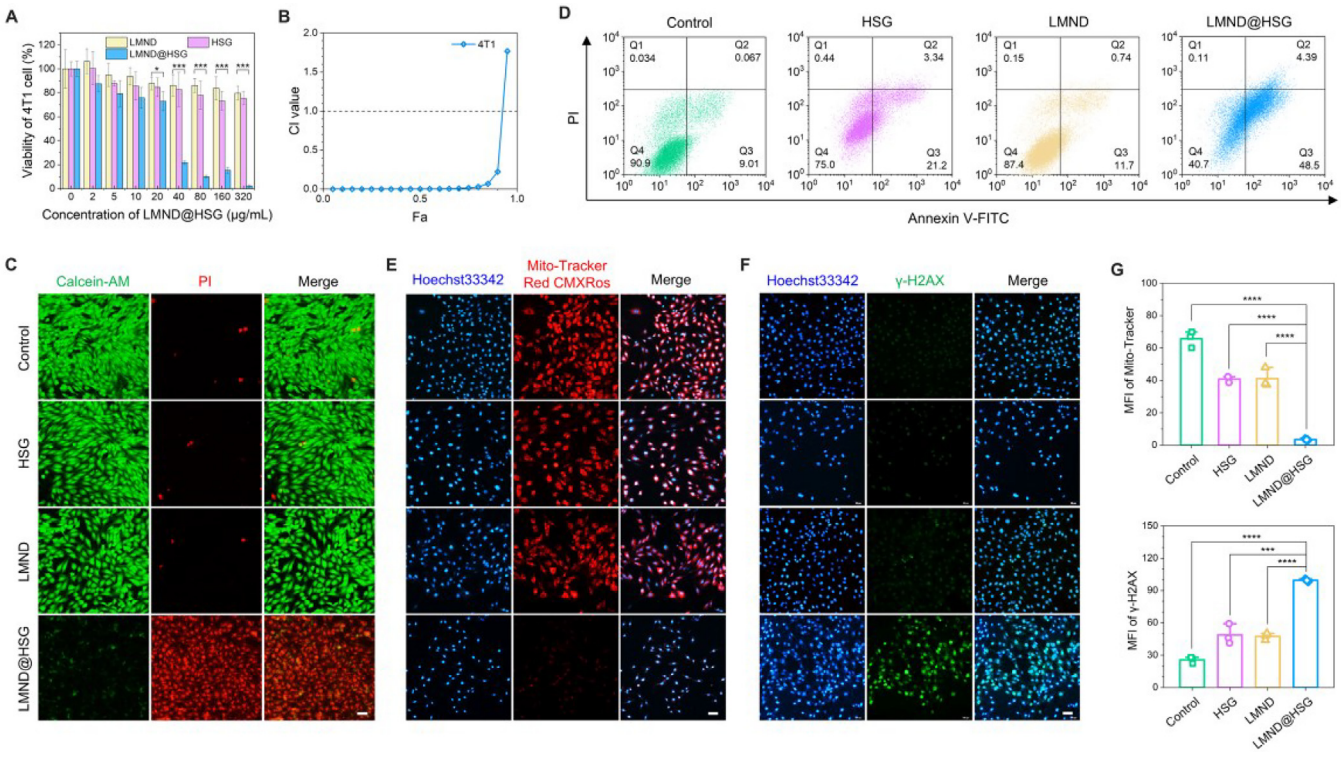

Fig. 5 – *In vitro* therapeutic performance of LMND@HSG. (A) *In vitro* cytotoxicity of LMND, HSG, and LMND@HSG toward 4T1 cells for 24 h. All data are expressed as mean ± SD ($n = 4$). *$P < 0.05$, ***$P < 0.001$. (B) CI values for the combination of HSG ligands and LMNDs. (C) Live/dead staining assay of 4T1 cells with LMND, HSG, and LMND@HSG incubations for 24 h. The live and dead cells were stained by green and red fluorescence, respectively. Scale bar: 50 μm. (D) Flow cytometric analysis of 4T1 cell apoptosis induced by LMND@HSG for 24 h using the Annexin V-FITC/PI staining. (E) Mitochondrial damage test in HSG, LMND and LMND@HSG-incubated 4T1 cells by Mito-Tracker (200 nM). Scale bar: 50 μm. (F) DNA damage test in HSG, LMND and LMND@HSG-incubated 4T1 cells by γ-H2AX Immunofluorescence. Scale bar: 50 μm. (G) MFI analysis of Mito-Tracker and γ-H2AX fluorescence staining in (D) and (E). All data are expressed as mean ± SD ($n = 3$). ***$P < 0.001$, ****$P < 0.0001$.

in Fig. 5B indicated the synergistic effect between LMND and HSG. Much research has demonstrated the synergistic therapeutic effect of ROS and NO. Zhao and Liu's groups both demonstrated that the synergistic therapy derived from both ROS and NO significantly suppressed the growth of cancer cells, offering new insights into NO gas therapy [40,41]. The *in vitro* cytotoxicity of LMND@HSG was also verified by Calcein AM/PI staining and Annexin V-FITC apoptosis kit tested by flow cytometry. At a feed concentration of 40 μg/ml, Calcein AM/PI staining results showed that LMND@HSG-treated group displayed overwhelming red fluorescence (>89%), indicating its high cytotoxicity, while the majority of 4T1 cells (96.3%, 97.8%) remained alive with treatments of LMND or HSG, respectively (Fig. 5C). Annexin V-FITC apoptosis detection showed that cell apoptotic ratio of LMND@HSG (52.9%) was much higher than those of other groups (LMND: 12.4%; HSG: 24.5%; Control: 9.1%) (Fig. 5D). All these results were consistent with those of the MTT tests.

It is known that NO could promote tumor growth at low concentrations [42]. When the concentration is over 1 μM, NO can destroy mitochondria and DNA through nitrification structure to inhibit tumor growth and metastasis [43]. Therefore, it is demanding to ensure enough NO could be released to induce cell death. Herein, HSG was selected as the stable ligand of LNMDs, in which guanidino groups act as the NO donors. Considering the IC50 value of LMND@HSG against 4T1 cells was 29.76 μg/ml, thus we utilized a higher concentration of LMND@HSG to perform *in vitro* assays (40 μg/ml), aiming to produce sufficient amounts of NO to exert anti-tumor effects, rather than promoting tumor growth.

Mito-Tracker Red CMXRos can stain normal mitochondria with strong red fluorescence, and the FI was negatively correlated with mitochondrial membrane potential, so the occurrence of cell apoptosis is usually accompanied by a decrease or the quench of the red fluorescence. As shown in Fig. 5E, the reduction of red fluorescence indicates that mitochondrial damage basically occurred in the LMND@HSG group but was not obvious in other groups. Moreover, the degree of DNA damage was also assessed by the DNA Damage Assay Kit by γ-H2AX immunofluorescence. The strongest green fluorescence was lit up in the LMND@HSG group, indicating significant DNA damage (Fig. 5F). The mean fluorescence intensity (MFI) of Mito-Tracker and γ-H2AX in the LMND@HSG group was significantly different compared to those of other groups (Fig. 5G). These results demonstrated that HSG@LMND nanomedicine could release both ROS and NO in tumor cells, simultaneously leading to DNA damage and mitochondrial dysfunction.

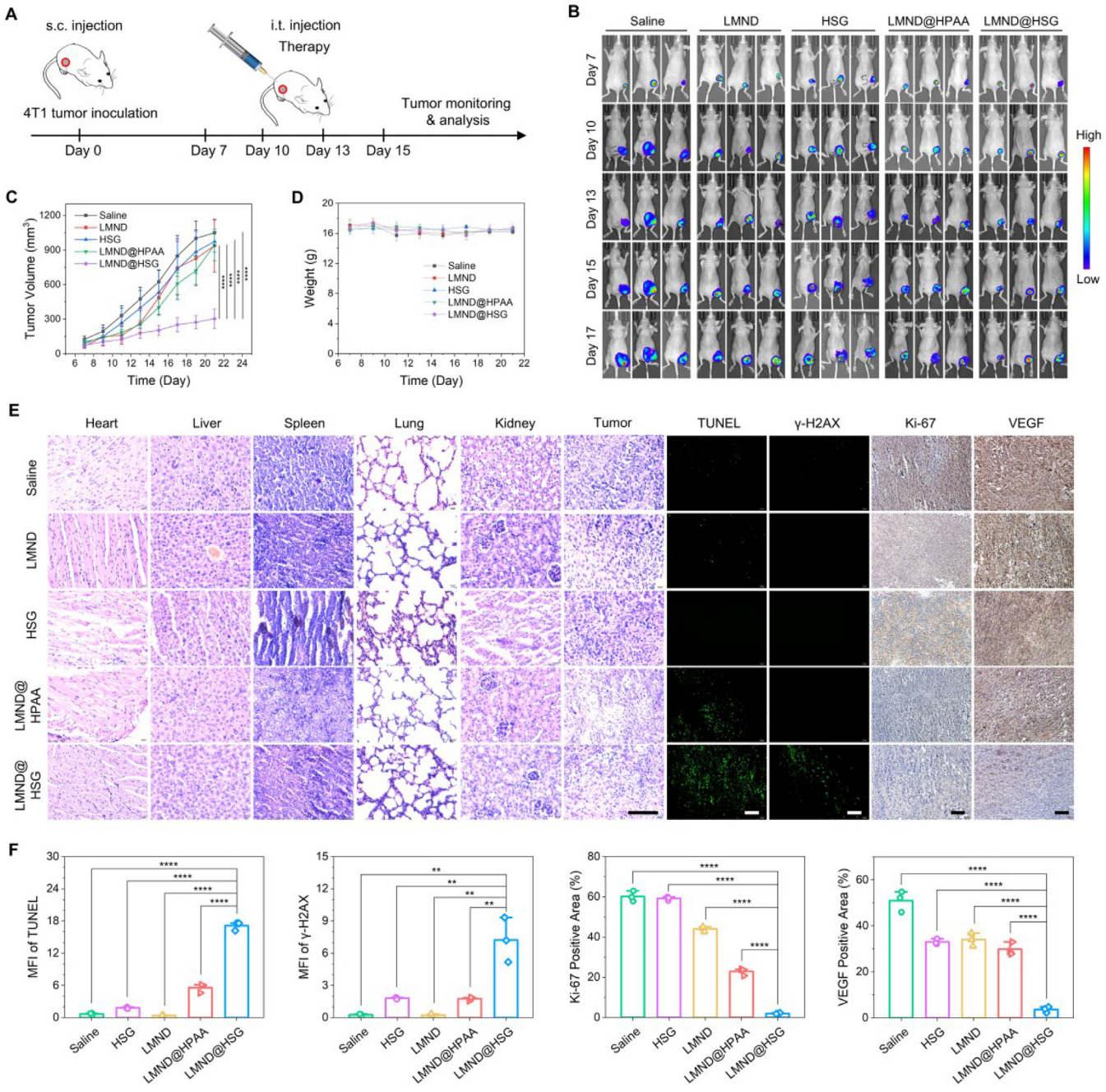

Fig. 6 – *In vivo* therapeutic efficacy of LMND@HSG. (A) Schematic diagram of the *in vivo* treatment in 4T1 xenograft mice models. (B) Dynamic IVIS imaging of mice with 4T1-luc tumor following different treatments. (C,D) Average tumor growth curves and body weight of mice receiving different treatments, saline, LMND (2 mg/kg), HSG (2 mg/kg), LMND@HPAA (2 mg/kg) and LMND@HSG (2 mg/kg). All data are represented as mean ± SD ($n = 6$). ****$P < 0.0001$. (E) H&E staining of major organs and tumor. TUNEL staining, γ-H2AX staining, immunohistochemical staining of Ki-67 and VEGF of 4T1 tumor sections. Scale bar: 100 μm. (F) Statistical analysis of IHC parameters (Ki-67 and VEGF) and MFI of TUNEL and γ-H2AX assays. All data are represented as mean ± SD ($n = 3$). **$P < 0.01$, ****$P < 0.0001$.

3.5. *In vivo therapeutic efficacy of LMND@HSG*

Next, the *in vivo* anticancer treatment efficacy of LMND@HSG was evaluated on a 4T1 tumor-bearing BALB/c nude mice model. No evident erythrocyte hemolysis was detected upon the interaction with LMND@HSG (Fig. S4). Since systemic administration could cause severe toxicity and promote new metastasis of breast cancer cells [44–45], intratumoral injection was utilized for further treatment in this study. The mice were divided into 5 groups: LMND, HSG, LMND@HPAA, LMND@HSG, and the saline control groups. These mice were locally administered with each formulation at the

same concentration of 2 mg/kg (Fig. 6A). The tumor growth evaluated by vernier caliper measurement was illustrated in Fig. 6C, LMND@HSG-treated group exhibited evident tumor growth suppression, while LMND, HSG and LMND@HPAA alone treatment could hardly take effect as the control. The dynamic bioluminescence signals collected at Day1, 4, 7, 9 and 11 post treatment from IVIS imaging also verified that LMND@HSG administration had the best antitumor efficacy (Fig. 6B). There were no evident weight losses in all groups of mice during the treatment period, which suggested good biocompatibility of all components for LMND@HSG (Fig. 6D). The mice were euthanized on Day14 post treatment when the tumor volume exceeded 1,000 mm^3, then tumor tissue and main organs (heart, liver, spleen, lung, and kidneys) of different groups were harvested for further characterization. Hematoxylin and eosin (H&E) staining images revealed no apparent damages or lesions in main organs (Fig. 6E). Additionally, the resected tumors were stained by dUTP-biotin nick end labeling (TUNEL) to estimate the degrees of necrosis and apoptosis. Fig. 6E and 6F showed that the treatment of LMND@HSG led to the most severe local necrosis in the tumor and achieved the most evident DNA damage through γ-H2AX staining. By contrast, LMND@HPAA could only trigger partial apoptosis but no obvious DNA damage, possibly because only ROS was involved in the treatment. Moreover, angiogenesis is one of typical characteristics of cancer. Some studies have demonstrated that the vascular endothelium growth factor (VEGF) has a significant impact in the progression of angiogenesis [46]. The immunohistochemical results of Ki-67 and VEGF revealed that tumor proliferation and angiogenesis were significantly inhibited upon LMND@HSG treatment. All these data reveal that the combined release of ROS and NO from LMND@HSG nanomedicine significantly enhanced cancer therapeutic efficacy.

It should be noted that ROS and NO both have a dual role in cancer development. ROS could exhibit both anti-apoptotic and pro-apoptotic effects. On one hand, the pro-apoptotic mechanism of ROS mainly includes cell cycle arrest, apoptosis, and necrosis. On the other hand, the anti-apoptotic effect promotes cell proliferation, invasion, and metastasis, while simultaneously inhibiting apoptosis [47]. Tumor cells often exhibit elevated ROS levels, which can drive proliferation and survival through various signaling pathways. Many cancer therapies aim to exploit the high ROS levels in cancer cells. For instance, radiation therapy generates ROS and leads to DNA damage in tumor cells. Chemotherapeutic agents, like doxorubicin, can also increase ROS levels, triggering apoptosis in cancer cells. Similarly, NO could participate in diverse physiological processes, such as vasodilation and immune response. Low concentrations of NO can promote tumor growth and angiogenesis and have cell-protective effects. High concentrations of NO exhibit cell cytotoxicity. The common mechanisms by which NO induces cell apoptosis involve activation of caspase, DNA fragmentation, and chromatin condensation [48]. Therefore, whether NO is anti-cancer or pro-cancer depends on its concentration, time and location [1,40,49]. Until now, a timely update of understanding NO and ROS remains necessary, helping researchers utilize the potential anticancer bioactivities of drugs that disrupt NO or ROS metabolism.

In view of the excellent performance of LMND@HSG *in vivo*, we delved into its potential immunotherapy effect and clinical translation. Until now, several approaches have been leveraged to trigger immunogenic cell death (ICD) in tumors to increase the immunogenicity of 'cold' tumor, such as glioblastoma [50], hepatocellular carcinomas [51], and breast cancer [52]. NO is one of the important therapeutic agents used to induce ICD. The high concentration of *in situ* generated NO can be utilized to increase the generation of tumor immune antigen [53], which could further enhance the development of antigen-presenting cells and activate T cells [54]. In future studies, the 4T1 model could be regarded as a 'cold' phenotype, exhibiting a low response to cancer immunotherapies [55,56], LMND@HSG could possibly improve the immunosuppressive microenvironment and enhance the tumor treatment efficacy by NO and ROS.

The simple chemical structure and composition of TME-responsive LMND@HSG NO nanogenerator, along with diverse properties including NO-potentiated tumor treatment, widely broaden the design strategies of nanomedicines and light up the prospect of the LMND@HSG system for clinical practice. However, several challenges remain to be addressed before the implementation. First, the biocompatibility of LMND should be systemically assessed. Both bulk LM and LMNDs are considered biocompatible, but current research on LM toxicity evaluation mainly relies on methods such as cytological experiments and serum chemistry, the option of representative animal models and specific mechanism studies are still rare [57]. Second, due to the complexity of the human immune system, there is limited information on the immune system's response to novel nanomedicines based on LMND [58], the immunogenicity and potential side effects should be comprehensively studied. Third, the *in vivo* metabolism of current LMND nanomedicines is a bit long. The plasma half-life of LMND usually exceeds 300 min, and Ga^{3+} ions could still be detected in the feces and urines of mice on Day 14 post intratumoral injection [31]. Therefore, issues such as surface properties, chemical structures, and administration methods need to be optimized.

4. Conclusion

In summary, a TME-responsive LMND-based gas nanogenerator was developed for NO-potentiated tumor treatment. The disulfide bonds initiated the GSH depletion and decomposition of HSG ligands in the TME, subsequently activating the degradation of LMND and leading to cascade generations of ROS and NO. Such features differentiated ROS-based LMND@HSG nanomedicine from prior studies and provided enhanced therapeutic efficacy, accompanied by the intrinsic anticancer activity of LMND. Moreover, the simple composition and diverse properties of LMND@HSG widely broaden the design strategies of nanomedicines for combination or synergistic therapy.

Conflicts of interest

The authors report no conflicts of interest. The authors alone are responsible for the content and writing of this article.

CRediT authorship contribution statement

Chen Su: Writing – review & editing, Writing – original draft, Methodology, Formal analysis, Data curation. **Jianhan Lin:** Writing – review & editing, Writing – original draft, Methodology, Investigation, Formal analysis. **Cong Li:** Writing – review & editing, Writing – original draft, Methodology, Investigation, Formal analysis. **Xinyu Wang:** Writing – review & editing, Writing – original draft, Methodology, Investigation, Formal analysis. **Donghui Pan:** Writing – review & editing, Writing – original draft, Methodology, Investigation, Formal analysis. **Lizhen Wang:** Writing – review & editing, Writing – original draft, Methodology, Investigation, Formal analysis. **Yuping Xu:** Writing – review & editing, Writing – original draft, Methodology, Investigation, Formal analysis. **Chongyang Chen:** Writing – review & editing, Writing – original draft, Methodology, Investigation, Formal analysis. **Kangfan Ji:** Writing – review & editing, Writing – original draft, Methodology, Investigation, Formal analysis. **Jinqiang Wang:** Writing – review & editing. **Daozhen Chen:** Writing – review & editing, Writing – original draft, Supervision, Project administration, Formal analysis, Conceptualization. **Min Yang:** Writing – review & editing, Writing – original draft, Project administration, Methodology, Formal analysis, Conceptualization. **Zhen Gu:** Writing – review & editing, Writing – original draft, Supervision, Project administration, Methodology, Conceptualization. **Junjie Yan:** Writing – review & editing, Writing – original draft, Visualization, Supervision, Project administration, Investigation, Funding acquisition, Conceptualization.

Acknowledgments

The authors are grateful for the support from the National Natural Science Foundation of China (22075114, 32371434, 82301630) and the Natural Science Foundation of Jiangsu Province (BK20211034). They also acknowledge the financial support from Jiangsu Provincial Medical Key Laboratory (Key Laboratory of Nuclear Medicine).

Supplementary materials

Supplementary material associated with this article can be found, in the online version, at doi:10.1016/j.ajps.2025.101018.

References

[1] Fukumura D, Kashiwagi S, Jain RK. The role of nitric oxide in tumour progression. Nat Rev Cancer 2006;6(7):521–34.
[2] Yu W, Jia F, Fu J, Chen Y, Huang Y, Jin Q, et al. Enhanced transcutaneous chemodynamic therapy for melanoma treatment through cascaded fenton-like reactions and nitric oxide delivery. ACS Nano 2023;17(16):15713–23.
[3] Huang Z, Fu J, Zhang Y. Nitric oxide donor-based cancer therapy: advances and prospects. J Med Chem 2017;60(18):7617–35.
[4] Wang Y, Yang T, He Q. Strategies for engineering advanced nanomedicines for gas therapy of cancer. Natl Sci Rev 2020;7(9):1485–512.
[5] Isenberg JS, Martin-Manso G, Maxhimer JB, Roberts DD. Regulation of nitric oxide signalling by thrombospondin 1: implications for anti-angiogenic therapies. Nat Rev Cancer 2009;9(3):182–94.
[6] Szabo C. Gasotransmitters in cancer: from pathophysiology to experimental therapy. Nat Rev Drug Discov 2016;15(3):185–203.
[7] Wan M, Chen H, Wang Q, Niu Q, Xu P, Yu Y, et al. Bio-inspired nitric-oxide-driven nanomotor. Nat Commun 2019;10(1):966.
[8] Wang K, Li Y, Wang X, Zhang Z, Cao L, Fan X, et al. Gas therapy potentiates aggregation-induced emission luminogen-based photoimmunotherapy of poorly immunogenic tumors through cGAS-STING pathway activation. Nat Commun 2023;14(1):2950.
[9] Yu L, Hu P, Chen Y. Gas-generating nanoplatforms: material chemistry, multifunctionality, and gas therapy. Adv Mater 2018;30(49):1801964.
[10] Fan W, Yung BC, Chen X. Stimuli-responsive NO release for on-demand gas-sensitized synergistic cancer therapy. Angew Chem Int Ed 2018;57(28):8383–94.
[11] Gehring J, Trepka B, Klinkenberg N, Bronner H, Schleheck D, Polarz S. Sunlight-triggered nanoparticle synergy: teamwork of reactive oxygen species and nitric oxide released from mesoporous organosilica with advanced antibacterial activity. J Am Chem Soc 2016;138(9):3076–84.
[12] Carpenter AW, Schoenfisch MH. Nitric oxide release: Part II. Therapeutic applications. Chem Soc Rev 2012;41(10):3742–52.
[13] Yang Y, Huang Z, Li L. Advanced nitric oxide donors: chemical structure of NO drugs, NO nanomedicines and biomedical applications. Nanoscale 2021;13(2):444–59.
[14] Wu X, Zhou Z, Li K, Liu S. Nanomaterials-induced redox imbalance: challenged and opportunities for nanomaterials in cancer therapy. Adv Sci 2024;11(16):2308632.
[15] Li S, Jiang P, Jiang F, Liu Y. Recent advances in nanomaterial-based nanoplatforms for chemodynamic cancer therapy. Adv Funct Mater 2021;31(22):2100243.
[16] Liang S, Liu Y, Zhu H, Liao G, Zhu W, Zhang L. In Emerging nitric oxide gas-assisted cancer photothermal treatment. Exploration 2024:20230163.
[17] Wang L, Ge K, Duan J, Du X, Zhou G, Ma L, et al. A double-gain theranostic nanoplatform based on self-supplying H_2O_2 nanocomposites for synergistic chemodynamic/gas therapy. J Colloid Interf Sci 2024;654:774–84.
[18] Fan WP, Lu N, Huang P, Liu Y, Yang Z, Wang S, et al. Glucose-responsive sequential generation of hydrogen peroxide and nitric oxide for synergistic cancer starving-like/gas therapy. Angew Chem Int Ed 2017;56(5):1229–33.
[19] Lin H, Chen Y, Shi JL. Nanoparticle-triggered *in situ* catalytic chemical reactions for tumour-specific therapy. Chem Soc Rev 2018;47(6):1938–58.
[20] Sun Z, Wang X, Liu J, Wang Z, Wang W, Kong D, et al. ICG/l-arginine encapsulated PLGA nanoparticle-thermosensitive hydrogel hybrid delivery system for cascade cancer photodynamic-NO therapy with promoted collagen depletion in tumor tissues. Mol Pharm 2021;18(3):928–39.
[21] Tang Y, Wang T, Feng J, Rong F, Wang K, Li P, et al. Photoactivatable nitric oxide-releasing gold nanocages for enhanced hyperthermia treatment of biofilm-associated infections. ACS Appl Mater Interfaces 2021;13(43):50668–81.

[22] Fang X, Cai S, Wang M, Chen Z, Lu C, Yang H. Photogenerated holes mediated nitric oxide production for hypoxic tumor treatment. Angew Chem Int Ed 2021;60(13):7046–50.
[23] Yan J, Lu Y, Chen G, Yang M, Gu Z. Advances in liquid metals for biomedical applications. Chem Soc Rev 2018;47(8):2518–33.
[24] Sun X, Yuan B, Sheng L, Rao W, Liu J. Liquid metal enabled injectable biomedical technologies and applications. Appl Mater Today 2020;20:100722.
[25] Yang N, Gong F, Zhou Y, Yu Q, Cheng L. Liquid metals: Preparation, surface engineering, and biomedical applications. Coordin Chem Rev 2022;471:214731.
[26] Wu Q, Xia N, Long D, Tan L, Rao W, Yu J, et al. Dual-functional supernanoparticles with microwave dynamic therapy and microwave thermal therapy. Nano Lett 2019;19(8):5277–86.
[27] Truong VK, Hayles A, Bright R, Luu TQ, Dickey MD, Kalantar-Zadeh K, et al. Gallium liquid metal: nanotoolbox for antimicrobial applications. ACS Nano 2023;17(15):14406–23.
[28] Liu Z, Tan X, Huang Y, Li W, Yang N, Yuan R, et al. Microwave absorption-based magnetic liquid metal nano-missiles for thermodynamic/immunological cascade hepatoma therapy. Chem Eng J 2023;471:144688.
[29] Li L, Chang H, Yong N, Li M, Hou Y, Rao W. Superior antibacterial activity of gallium based liquid metals due to Ga(3+) induced intracellular ROS generation. J Mater Chem B 2021;9(1):85–93.
[30] Yan J, Su C, Lou K, Gu M, Wang X, Pan D, et al. Constructing liquid metal/metal-organic framework nanohybrids with strong sonochemical energy storage performance for enhanced pollutants removal. J Hazard Mater 2023;452:131285.
[31] Yan J, Wang J, Wang X, Pan D, Su C, Wang J, et al. Activating tumor-selective liquid metal nanomedicine through galvanic replacement. Adv Mater 2024;36(5):2307817.
[32] Zhang C, Yang B, Biazik JM, Webster RF, Xie W, Tang J, et al. Gallium nanodroplets are anti-inflammatory without interfering with iron homeostasis. ACS Nano 2022;16(6):8891–903.
[33] Wan S, Zeng J, Cheng H, Zhang X. ROS-induced NO generation for gas therapy and sensitizing photodynamic therapy of tumor. Biomaterials 2018;185:51–62.
[34] Zhao Y, Shi D, Guo L, Shang M, Sun X, Meng D, et al. Ultrasound targeted microbubble destruction-triggered nitric oxide release via nanoscale ultrasound contrast agent for sensitizing chemoimmunotherapy. J Nanobiotechnol 2023;21(1):35.
[35] Xiong J, Yan J, Li C, Wang X, Wang L, Pan D, et al. Injectable liquid metal nanoflake hydrogel as a local therapeutic for enhanced postsurgical suppression of tumor recurrence. Chem Eng J 2021;416:129092.
[36] Yan J, Wang H, Zhou Q, You Y. Reversible and multisensitive quantum dot gels. Macromolecules 2011;44(11):4306–12.
[37] Ferruti P, Marchisio MA, Duncan R. Poly(amido-amine)s: biomedical applications. Macromol Rapid Commun 2002;23(5-6):332–55.
[38] Perikala M, Bhardwaj A. Excellent color rendering index single system white light emitting carbon dots for next generation lighting devices. Sci Rep 2021;11(1):11594.
[39] Parikh SJ, Chorover JJL. ATR-FTIR spectroscopy reveals bond formation during bacterial adhesion to iron oxide. Langmuir 2006;22(20):8492–500.
[40] Xu W, Liu LZ, Loizidou M, Ahmed M, Charles I. The role of nitric oxide in cancer. Cell Res 2002;12(5):311–20.
[41] Shi H, Xiong CF, Zhang LJ, Cao HC, Wang R, Pan P, et al. Light-triggered nitric oxide nanogenerator with high l-arginine loading for synergistic photodynamic/gas/photothermal therapy. Adv Healthc Mater 2023;12(20):2300012.
[42] Cao Y, Liu M, Cheng J, Yin J, Huang C, Cui H, et al. Acidity-triggered tumor-targeted nanosystem for synergistic therapy via a cascade of ROS generation and NO release. ACS Appl Mater Interfaces 2020;12(26):28975–84.
[43] Deng Y, Jia F, Chen X, Jin Q, Ji J. ATP Suppression by pH-activated mitochondria-targeted delivery of nitric oxide nanoplatform for drug resistance reversal and metastasis inhibition. Small 2020;16(23):2001747.
[44] Peng F, Setyawati MI, Tee JK, Ding X, Wang J, Nga ME, et al. Nanoparticles promote *in vivo* breast cancer cell intravasation and extravasation by inducing endothelial leakiness. Nat Nanotechnol 2019;14(3):279–86.
[45] Zhao Z, Ukidve A, Kim J, Mitragotri S. Targeting strategies for tissue-specific drug delivery. Cell 2020;181(1):151–67.
[46] Alsaab HO, AS Al-Hibs, Alzhrani R, Alrabighi KK, Alqathama A, Alwithenani A, et al. Nanomaterials for antiangiogenic therapies for cancer: a promising tool for personalized medicine. Int J Mol Sci 2021;22(4):1631.
[47] Glorieux C, Liu S, Trachootham D, Huang P. Targeting ROS in cancer: rationale and strategies. Nat Rev Drug Discov 2024;23:583–606.
[48] Reddy TP, Glynn SA, Billiar TR, Wink DA, Chang JC. Targeting nitric oxide: Say no to metastasis. Clin Cancer Res 2023;29(10):1855–68.
[49] Hu Y, Xiang J, Su L, Tang X. The regulation of nitric oxide in tumor progression and therapy. J Int Med Res 2020;48(2):0300060520905985.
[50] You H, Geng S, Li S, Imani M, Brambilla D, Sun T, et al. Recent advances in biomimetic strategies for the immunotherapy of glioblastoma. Biomaterials 2024;311:122694.
[51] Chen K, Shuen TW, Chow PK. The association between tumour heterogeneity and immune evasion mechanisms in hepatocellular carcinoma and its clinical implications. Br J Cancer 2024;131:420–9.
[52] Yang L, Hu Q, Huang T. Breast cancer treatment strategies targeting the tumor microenvironment: how to convert “cold” tumors to “hot” tumors. Int J Mol Sci 2024;25(13):7208.
[53] Jiang W, Dong W, Li M, Guo Z, Wang Q, Liu Y, et al. Nitric oxide induces immunogenic cell death and potentiates cancer immunotherapy. ACS Nano 2022;16(3):3881–94.
[54] Krysko DV, Garg AD, Kaczmarek A, Krysko O, Agostinis P, Vandenabeele P. Immunogenic cell death and damps in cancer therapy. Nat Rev Cancer 2012;12(12):860–75.
[55] Wu Y, Zhang C, Liu X, He Z, Shan B, Zeng Q, et al. ARIH1 signaling promotes anti-tumor immunity by targeting PD-L1 for proteasomal degradation. Nat Commun 2021;12(1):2346.
[56] Rupp T, Genest L, Babin D, Legrand C, Hunault M, Froget G, et al. Anti-CLTA-4 and anti-PD-1 immunotherapies repress tumor progression in preclinical breast and colon model with independent regulatory T cells response. Transl Oncol 2022;20:101405.
[57] Xu H, Lu J, Xi Y, Wang X, Liu J. Liquid metal biomaterials: translational medicines, challenges and perspectives. Natl Sci Rev 2024;11(2):nwad302.
[58] Mundekkad D, WCJIjoms Cho. Nanoparticles in clinical translation for cancer therapy. Int J Mol Sci 2022;23(3):1685.